Structural phase transition of ultra thin PrO_2 films on Si(111)

2009 J. Phys.: Condens. Matter 21 175408

(http://iopscience.iop.org/0953-8984/21/17/175408)

J. Phys.: Condens. Matter **21** (2009) 175408 (8pp) doi:10.1088/0953-8984/21/17/175408

Structural phase transition of ultra thin PrO_2 films on Si(111)

S Gevers, T Weisemoeller, B Zimmermann, F Bertram, C Deiter[1] and J Wollschläger

Fachbereich Physik, Universität Osnabrück and Center of Interface Science, Barbarastraße 7, 49069 Osnabrück, Germany

E-mail: joachim.wollschlaeger@uni-osnabrueck.de

Received 23 January 2009, in final form 10 March 2009
Published 30 March 2009
Online at stacks.iop.org/JPhysCM/21/175408

Abstract

Ultra thin heteroepitaxial PrO_2 films on Si(111) were annealed under UHV conditions and investigated by x-ray diffraction (XRD), x-ray reflectometry (XRR) and spot profile analysis low energy electron diffraction (SPALEED) with regard to structural stability and phase transitions due to the high oxygen mobility of the oxide. This gives information about the manageability of the material and its application as a model catalyst system in surface science. While the samples are stable in UHV at room temperature, annealing at 300 °C exhibits a terminated phase transition from PrO_2 and $PrO_{2-\Delta}$ to cub-Pr_2O_3 with an increase in the silicate at the interface and a decrease in the crystalline praseodymia layer mainly due to atomic diffusion of silicon into the oxide film. Strain effects during the phase transition also cause mosaic formation at the surface. Further annealing up to 600 °C shows only little change in the film structure. This will finally lead to a model of the film structure during the annealing process.

(Some figures in this article are in colour only in the electronic version)

1. Introduction

Today, about 90% of all chemical reactions are driven by heterogeneous catalysis [1]. In this context, rare earth oxides are of interest due to their high oxygen mobility and storage capability [2–4]. In particular praseodymium oxides are in the focus of both industrial and scientific research because of their high C_2 selectivity for the oxidative coupling of methane [5] so that the formation of ethane (C_2H_6) and ethylene (C_2H_4) during the catalytic process is increased compared to the formation of CO_2. This offers attractive applications in the field of ethane and ethylene synthesis [6].

Since important details of these catalytic processes are not well understood yet, simplified model systems are necessary to learn more about oxygen transport and transfer in praseodymium oxide based catalytic reactions. Thin and highly ordered two-dimensional oxide films on well known substrates could be used for that purpose as they have already been applied with oxide films on metal substrates [7, 8]. Heteroepitaxial PrO_2 films on Si(111) can be applied to form such a model system since they can be easily prepared to a high quality by pulsed laser deposition (PLD) [9] or alternatively by O_2-annealing of praseodymium sesquioxide film with hexagonal structure (hex-Pr_2O_3) deposited by molecular beam epitaxy (MBE) [10].

Praseodymia films also offer applications within the field of micro- and nanoelectronics. Here, germanium on insulator (GeOI) technology can be used for cost-effective integration of III–V optoelectronic materials like GaAs on the dominating Si material platform, since the lattice mismatch between GaAs and Ge is only 0.08% [11]. In this case it has been demonstrated that high quality praseodymia films serve well as insulating buffer films, because these dielectric heterostructures can be achieved with low defect levels on Si(111) [12].

The present work seeks to verify the structural stability of praseodymia films during annealing in UHV and also to establish the appearance of phase transitions which may occur due to oxygen loss. For this purpose x-ray reflectometry (XRR) and x-ray diffraction (XRD) as well as spot profile low energy electron diffraction (SPALEED) studies were performed.

[1] Present address: HASYLAB, DESY, Hamburg, Germany.

2. Experiment

Ultra thin films of hex-Pr_2O_3 structure with 10 nm film thickness were deposited on clean boron-doped Si(111) substrates as reported in [13]. These samples were oxidized by annealing in 1 atm oxygen at 700 °C for 30 min. This treatment leads to heteroepitaxial praseodymia films with a fluorite structure ($Fm\bar{3}m$ in Hermann–Mauguin notation) and lattice constants close to bulk $PrO_2(111)$ [10]. Afterwards the samples were annealed in ultra high vacuum (UHV, base pressure 1×10^{-10} mbar) at temperatures from $T = 300$ to 600 °C. The annealing was performed by resistive heating of the samples.

X-ray measurements for determination of the oxide film structure were performed at beamline W1/HASYLAB. A six-circle diffractometer with horizontal alignment of the sample and a photon energy of 10.5 keV was used to conduct XRR and XRD measurements. In both cases the data were recorded with θ–2θ scans.

In order to study the surface structure and morphology, SPALEED investigations were carried out in UHV. These measurements were performed after each annealing step with the sample aligned normal to the incident electron beam. For reasons of comparability the distances within these diffraction patterns are always labeled corresponding to the pattern of the substrate (hexagonal Si(111)-7 × 7 surface). Furthermore, energy dependent measurements of the intensity of the specular diffraction peak were made (with steps $\Delta T_A = 100 \pm 30$ °C for the annealing temperature) to perform a spot profile analysis.

3. Results

3.1. XRD and XRR

Figure 1 presents θ–2θ scans recorded from praseodymia films after different treatments. L denotes the scattering vector normal to the surface with reciprocal lattice units (r.l.u). Thus the Bragg peaks denoted by $(00L)_S$ in surface notation are equivalent to the $(LLL)_B$ Bragg peaks in bulk notation due to the (111) orientation of the silicon substrate.

Scan (A) shows the XRD pattern of the sample directly after preparation of the praseodymia film. It exhibits three strong and sharp Bragg peaks due to the *semi-infinite* Si(111) substrate, since the penetration depth of the x-ray beam is much larger than the thickness of the ultra thin praseodymium oxide film. The peaks at $L = 1$ and 3 are allowed within the kinematic diffraction theory for the diamond structure of Si. The weaker peak at $L = 2$, which is kinematically forbidden for the diamond structure, is caused by the non-spherical charge distribution of Si atoms. As the thickness of the silicon is *semi-infinite*, this Bragg peak is much sharper than the Bragg peak of the PrO_2 *film*. Hence the sharp but weak Si Bragg peak can be used for calibration of the additional broader Bragg peaks caused by praseodymia films. Strong PrO_2 peaks can be observed close to all integer L values due to the fluorite structure of PrO_2. Furthermore, interference effects between film and substrate occur near both the $Si(001)_S$ and $Si(003)_S$ Bragg peaks. Additional weak Bragg peaks are at half integer positions for the non-annealed samples. These peaks

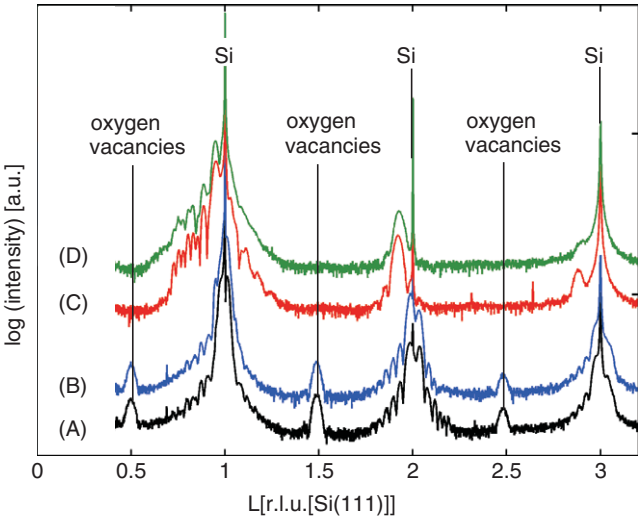

Figure 1. Specular XRD θ–2θ scans of the 10 nm praseodymia films on Si(111): (A) as-deposited; (B) after 8 h in UHV; (C), (D) after annealing at 300 °C and 600 °C, respectively, in UHV.

are caused by structures whose vertical lattice spacing is about twice as large as the PrO_2 bulk value and so they cannot be attributed to PrO_2 films with perfect fluorite structure. The hex-Pr_2O_3 structure, which would exhibit Bragg peaks at $L = 0.52$, 1.56 and 2.56, can also be excluded. However, it is known that PrO_2 can only completely be oxidized at high oxygen pressure so it tends to form oxygen vacancies without rearrangement of the praseodymium atoms [18]. As suggested by [10], the peaks at half integer L values point to oxygen vacancies missing in every second layer so that periodicity of $PrO_{2-\Delta}$ in the vertical direction is twice the lattice spacing of PrO_2.

The comparison between the XRD experiments on samples (A) and (B) (sample after 8 h under UHV conditions at room temperature) exhibits no significant differences. Thus the PrO_2 film is stable under UHV conditions. After annealing (samples (C) and (D)) the peaks at half-integer positions have vanished and the other Bragg peaks due to praseodymia are shifted to lower L values (as seen particularly well close to $L = 2$). Therefore the lattice spacing increases after annealing. Furthermore, strong interference effects at $L \approx 1$ are visible.

For analysis of the peak profiles a closer look at $L \approx 2$ is shown in figure 2(a). This position is used because the interference effects between oxide film and substrate signal are negligible and the diffracted intensities of both silicon substrate and praseodymia film are still sufficient. Thus the $Si(002)_S$ peak is used as a marker to determine precisely both the position of the Bragg peaks and the lattice spacing of the praseodymia films. The interface distance, however, cannot be determined.

For the untreated sample (figure 2(a), sample (A)) the diffracted intensity close to $L = 2$ consists of a sharp $Si(002)_S$ peak at $L = 2$ and two broader signals due to the oxide film. Furthermore, additional fringes are observed in this region demonstrating the high homogeneity of the praseodymia films.

Figure 2(a) also shows the Bragg peak positions (dashed lines) for bulk PrO_2, Pr_6O_{11} and cub-Pr_2O_3 (praseodymium oxide with cubic (bixbyite) structure) [14]. It can be seen that

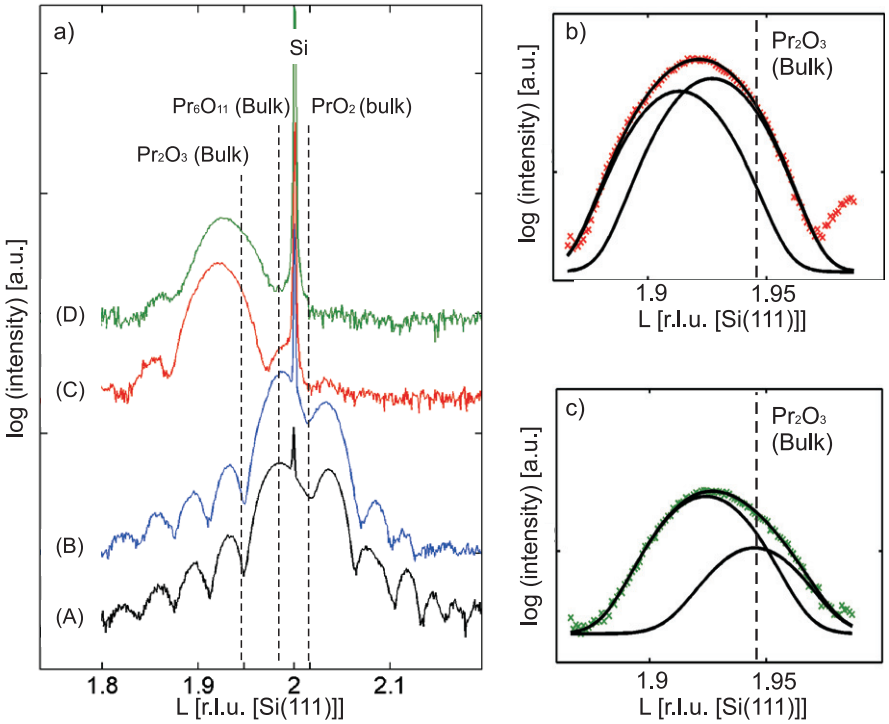

Figure 2. (a) Detailed view of the specular θ–2θ scans close to $L = 2$. Dashed lines indicate the positions of PrO_2, Pr_6O_{11} and cub-Pr_2O_3 Bragg peaks (bulk values). (b), (c) Detailed analysis of the oxide film peaks after annealing at 300 °C and 600 °C, respectively. Solid lines represent the fitted Gaussian functions.

after sample preparation one of the measured Bragg positions exhibits good agreement with the Pr_6O_{11} structure, but as shown in [10] it is difficult to obtain the specific stoichiometric phase in this region due to lateral strain effects caused by the substrate. Thus this peak may also be identified with a non-stoichiometric $PrO_{2-\Delta}$ phase. The other peak is located close to the bulk value of the PrO_2 structure (−1% mismatch compared with bulk PrO_2), with a slight shift to higher L values. After annealing of the sample the shifted peaks can be found close to the bulk position of cub-Pr_2O_3, but they are partially shifted to lower L values (about +1.7% mismatch with respect to bulk cub-Pr_2O_3). As will be discussed in detail later on, this effect is due to vertical distortion of the oxide film. The phase transition from PrO_2 to cub-Pr_2O_3 is confirmed by SPALEED (see below).

The two Bragg peaks of samples (A) and (B), respectively, can be fitted well assuming Gaussians. Peak positions of $L_1 = 1.987$ and $L_2 = 2.033$ are obtained for the oxide film. This is equivalent to two different oxide lattice spacings of $a_{\perp,1} = 3.155 \pm 0.001$ Å and $a_{\perp,2} = 3.084 \pm 0.001$ Å for $PrO_{2-\Delta}$ and PrO_2, respectively.

From the FWHM of the oxide Bragg peaks we obtain thicknesses of $D_1 = 8.6 \pm 0.5$ nm ($PrO_{2-\Delta}$) and $D_2 = 9.6 \pm 0.5$ nm (PrO_2) for the *crystalline* film of sample (A). The storage of the sample in UHV (sample B) does not lead to significant profile changes of the diffracted intensity. After annealing at 300 °C (sample C) it seems as though only one oxide peak, shifted to a lower L value, remains. However, a detailed profile analysis shows that two Gaussians are necessary to obtain good agreement between the experimental data and the optimized intensity calculations (cf figure 2(b)). The peak positions are $L_3 = 1.927$ and $L_4 = 1.913$ which result in vertical lattice spacings of $a_{\perp,3} = 3.254 \pm 0.001$ Å and $a_{\perp,4} = 3.277 \pm 0.001$ Å. The resulting film thicknesses are $D_{3,4} = 7.2 \pm 0.5$ nm. Further annealing at 600 °C (sample (D)) leads to a small decrease of the lattice spacings to $a_{\perp,3} = 3.223 \pm 0.001$ Å and $a_{\perp,4} = 3.258 \pm 0.001$ Å (cf figure 2(c)) and an additional decrease of the film thickness to $D_{3,4} = 6.7 \pm 0.5$ nm. It can be seen that the vertical lattice spacings are larger than the theoretical bulk values of cub-Pr_2O_3. This is due to homogeneous distortions in the lateral direction which lead to a vertical expansion of the unit cell (tetragonal distortion) [10]. Since the distortion during the phase transition is unequal for PrO_2 and $PrO_{2-\Delta}$, there are still two structure species observable after phase transition which will be explained in detail later.

The XRR results, presented in figure 3(a), exhibit strong intensity oscillations for the sample stored under UHV (sample B). These oscillations are damped after annealing at 300 °C (sample (C)) for large scattering vectors $Q_\perp$ pointing to increasing interface roughness with increasing annealing temperature. Further annealing at 600 °C (sample D) shows an enhanced intensity attenuation. Careful analysis of the data demands that in all cases the oxide film consists of two different species (two-column model, cf figure 7). Furthermore, the XRR analysis demonstrates that an amorphous silicate film is formed at the interface between praseodymia film and Si substrate. Figure 3(b) shows that the film thickness of the crystalline oxide species decreases by about $\Delta D_1 = 1.7$ nm and $\Delta D_2 = 2.3$ nm during the

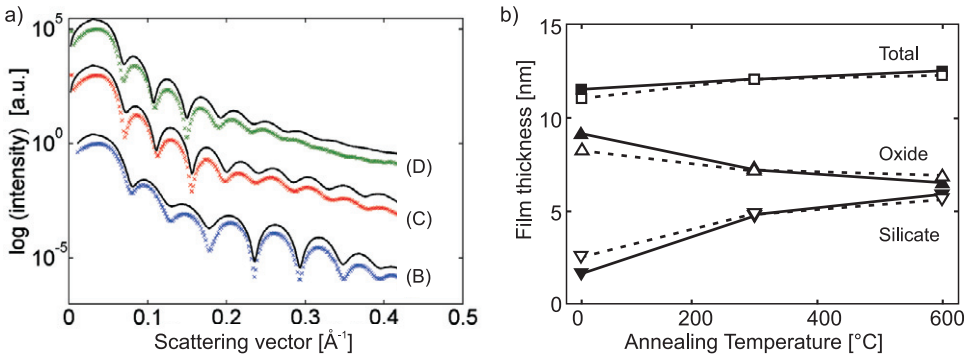

Figure 3. (a) XRR spectra of sample (B) after UHV-storage and samples (C) and (D) after annealing at 300 °C and 600 °C in UHV, respectively. The fitted data are represented by solid lines. These lines are shifted vertically for clarity. (b) Film thicknesses of the oxide layer and the silicate at the interface during sample annealing. The different oxide species are identified with filled and open markers.

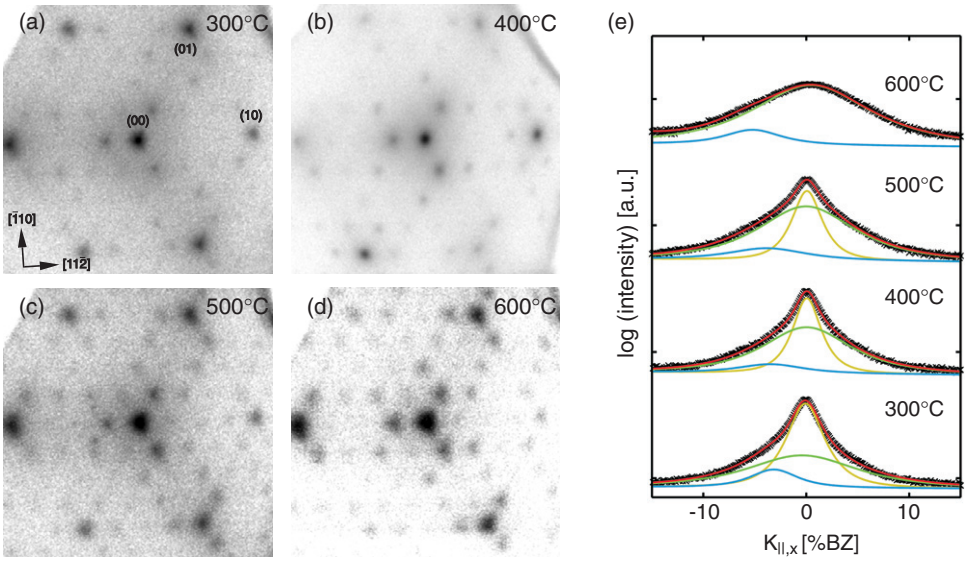

Figure 4. (a)–(d) SPALEED patterns obtained after annealing the samples at different temperatures. The crystallographic directions and denotations of the diffraction peaks are given in (a). Profiles of the (00)-diffraction peaks corresponding to (a)–(d) are shown in (e). Solid lines represent the Lorentzian functions which are necessary to fit the data.

annealing process. This is in good agreement with the XRD data. The silicate interfaces between the species and the substrate increase simultaneously by about $\Delta I_1 = 3.5$ nm and $\Delta I_2 = 3.7$ nm. Therefore the crystalline praseodymia film is partially consumed during the annealing process via formation of the silicate interface film.

3.2. SPALEED

Figures 4(a)–(d) show two-dimensional electron diffraction patterns of praseodymia films recorded at an electron energy of 57.8 eV after annealing the samples at temperatures from 300 to 600 °C with annealing temperature steps of $\Delta T = 100$ °C. Strong 'fundamental' diffraction peaks with a three-fold symmetry are visible in each diffraction pattern which can be attributed to PrO_2. Additional peaks within the surface Brillouin zone (SBZ) can be observed, too. The distance between these peaks is four times smaller than the distance between the 'fundamental' peaks. As the cub-$Pr_2O_3(111)$ surface unit cell in real space is four times larger (bixbyite structure) than the $PrO_2(111)$ surface unit cell (fluorite structure), these diffraction patterns confirm the phase transition from PrO_2 to cub-Pr_2O_3 for the surface as demonstrated before by XRD for the bulk of the praseodymia film. Furthermore, they show a three-fold symmetry. During the annealing process the (00)-diffraction peak broadens and after annealing at 500 °C the peak profile exhibits a star-like shape. In addition, the peaks within the PrO_2 SBZ become more pronounced during annealing until 500 °C is reached.

Figure 4(e) shows cross sections (line scans) in the [10]-surface direction (equivalent to [11$\bar{2}$]-bulk direction) of the (00)-diffraction peaks presented in figures 4(a)–(d). $K_\parallel$ denotes the parallel component of the scattering vector. After annealing at 300 °C the profile can be fitted with three Lorentzian functions. Two functions (yellow, green) with different FWHMs but the same peak positions at $K_\parallel = 0$ are necessary for the (00)-diffraction peak itself. This is due to the incoherent intensity interference of two oxide species with different surface morphologies. In the following the species

which cause the sharper Lorentzian is denoted by species 1 and the other by species 2. One additional Lorentzian (blue) has to be added at $K_{\parallel} \neq 0$ for a star-like shoulder which cannot be seen in the 2D-diffraction pattern since its intensity is very weak. The same profile can be resolved after annealing at 400 and 500 °C. The shoulder due to the star-like shape, however, shifts to larger $K_{\parallel}$ values and finally becomes visible in the diffraction pattern (cf figure 4(d)). After annealing to 600 °C the sharp Lorentzian function at $K_{\parallel} = 0$ vanishes and only the broad Lorentzian remains.

The FWHM analysis of the (00)-diffraction peak recorded at various vertical scattering vectors ($K_{\perp}$) can be seen in figures 5(a) and (b), respectively, for the annealing steps at 300 and 600 °C. The results for the annealing steps at 400 and 500 °C are comparable with (a). The analysis in (a) shows the FWHM for both Lorentzian functions at $K_{\parallel} = 0$. An oscillatory behavior can be observed in both cases. Furthermore, an additional linear increase of the FWHM is also visible. In figure 5(b) the broad Lorentzian function remaining after annealing at 600 °C also exhibits an oscillatory behavior of the FWHM added to a linear increase. Generally speaking, the linear increase is due to mosaics while the oscillations of the FWHM are due to mono-atomic steps [15].

The FWHM curves are fitted with a cosine function [15] with an additional linear function due to mosaics:

$$\mathrm{FWHM[\%SBZ]} = 100\%\mathrm{SBZ}\left[\frac{1-\cos(K_{\perp}d)}{\langle\Gamma\rangle\pi a} + \frac{K_{\perp}d\Delta\vartheta}{\sqrt{2}\pi}\right].$$

The step height, the mosaic spread, the mean terrace width and the lateral lattice constant are denoted by d, $\Delta\vartheta$, $\langle\Gamma\rangle$ and a, respectively. Figures 6(a)–(c) show the obtained fitting parameters. The step heights (a) at the surface after annealing at 300 °C are $d_1 = 3.16$ Å for species 1 and $d_2 = 3.10$ Å for species 2. After annealing at 400 °C both distances increase to values of $d_1 = 3.21$ Å and $d_2 = 3.18$ Å, respectively. These values remain nearly constant during the further annealing process. The comparison between the theoretical bulk values ($d_{PrO_2} = 3.08$ Å, $d_{\mathrm{cub-}Pr_2O_3} = 3.22$ Å) and the measured data show that the lattice spacings tend to be closer to the PrO_2 structure after annealing at 300 °C, although the diffraction pattern points to the formation of cub-Pr_2O_3. With further annealing up to 600 °C the distances increase. Thus they are closer to the cub-Pr_2O_3 structure. The mosaic spread (b) exhibits two different values for both species which remain constant during annealing. The mean values are $\Delta\vartheta_1 = 0.19°$ for the sharp Lorentzian function and $\Delta\vartheta_2 = 0.86°$ for the broader part. The mean terrace widths also exhibit two different values. The average terrace width of species 1 stays nearly constant with a mean value of $\langle\Gamma\rangle_1 = 31$ Å, but the value for species 2 increases slightly from $\langle\Gamma\rangle_2 = 10$ to 19 Å. As the sharp Lorentzian contribution to the peak in figure 4 is vanishing after annealing at 600 °C, only one value can be resolved for all investigated surface parameters (cf figures 6(a)–(c)).

4. Discussion

The results presented in this work lead to a model of the annealing process which is shown schematically in figure 7.

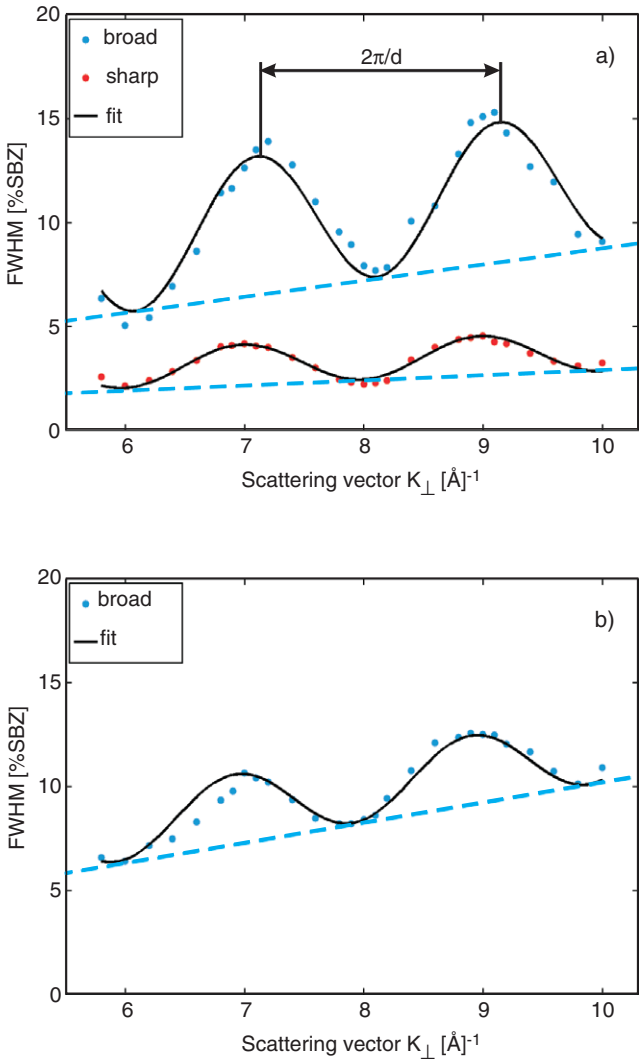

Figure 5. Example data of the FWHM dependency against the scattering phase: (a) after annealing at 300 °C and (b) after annealing at 600 °C. Dashed lines indicate the linear increase of the FWHM due to mosaics on the surface.

The initial film structure (figures 7(a) and (b)) consists of the crystalline praseodymia film split into a PrO_2 and a $PrO_{2-\Delta}$ species as found by the peak positions in XRD measurements [10]. $PrO_{2-\Delta}$ has the larger lattice spacing since the loss of oxygen is accompanied by the generation of Pr^{3+} ions which are larger than Pr^{4+} ions. Both species coexist laterally so that grains of both species have the thickness of the film (two-column model). A model with vertical stacking of both species (vertical coexistence) can be excluded due to the comparison between the film thicknesses obtained from XRR and XRD. Furthermore, the $PrO_{2-\Delta}$ species is responsible for the superstructure peaks found in figure 1, curves (A) and (B), as a result of periodically arranged oxygen vacancies. An example of this effect is shown in figure 7(a) and discussed in detail in [10]. The observed smaller lattice spacing of the PrO_2 film compared to bulk PrO_2 can be explained with lateral strain effects. Laterally the surface unit cell of PrO_2(111) is pinned to the bigger size of hex-Pr_2O_3(111) due to the preparation

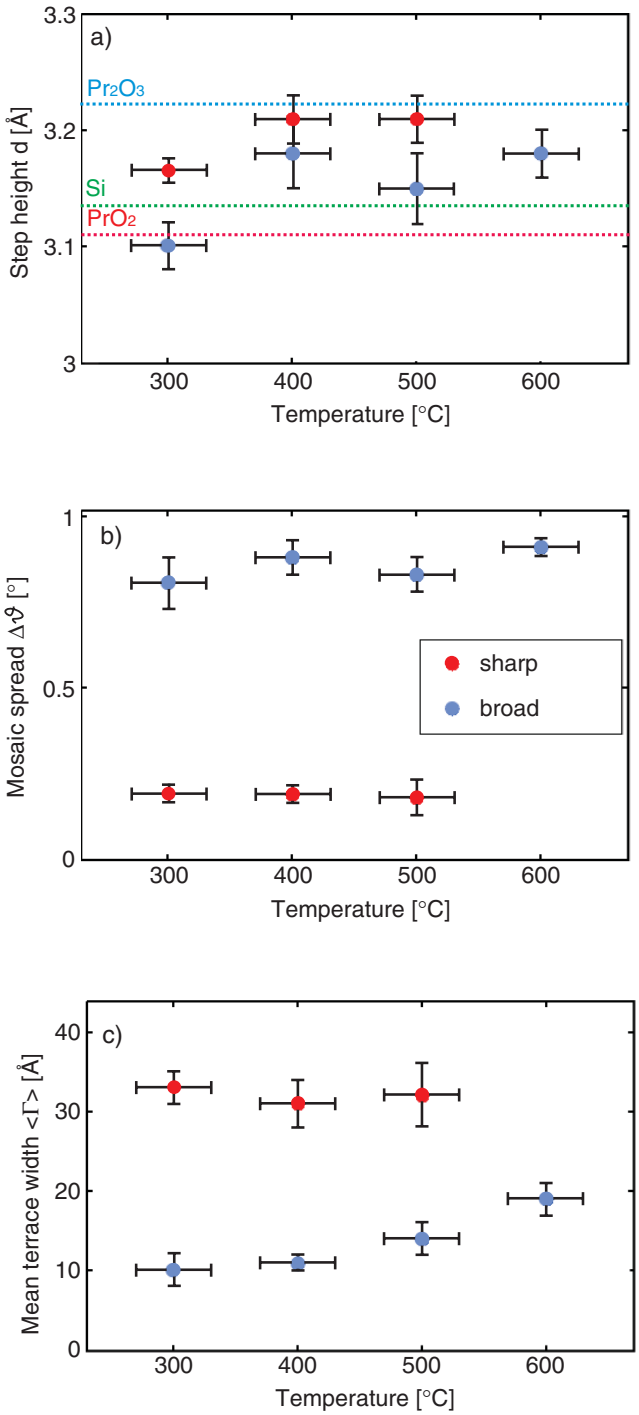

Figure 6. Data obtained from the FWHM analysis against the annealing temperatures: (a) lattice spacings (dotted lines indicate the theoretical bulk values of Si(111), PrO_2 and cub-Pr_2O_3); (b) mosaic spreads; (c) mean terrace widths.

process. Therefore the film has to contract vertically due to the elastic deformation [10]. The third component of the film system can be identified with a silicate film at the interface. This interface is formed during annealing of the hex-Pr_2O_3 in oxygen to form the PrO_2 film as reported in [16].

Both the vertical lattice spacings of 3.254 and 3.277 Å measured by XRD for the annealed film and the additional 2D-diffraction pattern with peaks at positions expected for cub-Pr_2O_3 obtained with SPALEED suggest a complete phase transition of the crystalline oxide layer into cub-Pr_2O_3 after annealing of the PrO_2 films at 300 °C in UHV.

However, there is a discrepancy between this and the respective step heights obtained from the SPALEED measurements ($d_1 = 3.16$ Å and $d_2 = 3.10$ Å), which are closer to the PrO_2 phase. Both techniques, however, are sensitive to different parts of the film. While electron diffraction probes only the region close to the surface of the film, x-ray diffraction probes the entire film (and the substrate). Therefore, it seems that there is still an appreciable amount of crystalline PrO_2 at the surface, but this would be inconsistent with the XRD experiment. On the one hand, surface energy effects can decrease the distance between the topmost atomic layers. This is also reported for ultra thin hex-Pr_2O_3 films on Si(111) by [17]. Here, the top lattice spacing decreased by about 5% compared to the bulk value which is comparable to the data obtained after annealing at 300 °C with SPALEED (1.9% and 3.7% compared to $d_{\text{bulk}} = 3.22$ Å). Further annealing leads to a relaxation of the step heights, as can be seen in the SPALEED data, where still smaller step heights are observed compared to the lattice spacing obtained from XRD. On the other hand, it is assumed that hydroxides ($Pr(OH)_3$) and carbon compounds (PrC_2) which contaminate the oxide surface desorb at the temperature regime close to 300 °C [19]. This can also be responsible for smaller lattice spacings than the bulk value at the surface due to the strong disorder in cub-Pr_2O_3.

It becomes clear that the two-column model is still applicable for the obtained data after the phase transition by comparing the film thickness calculated with XRR and XRD. As discussed in [18], a stoichiometric lattice composition is the exception rather than the rule. Based on this fact the formation of two non-stoichiometric cub-Pr_2O_3 phases is probable due to unequal structural changes of the two initial oxide species PrO_2 and $PrO_{2-\Delta}$ to cub-Pr_2O_3. This also explains the varying surface morphologies determined with SPALEED and the differing lattice spacings. The binding at the interface pins the lateral positions of the oxide ions. The resulting strain causes the vertical expansion of the oxide film, since the bulk lattice constant is increased due to oxygen removal (see above) so that the strain increases for the pinned oxide film. This strain leads to vertical deformations at the surface of the film (cf figure 7(b)) and forms the two mosaic regimes as well as the lattice spacings, as determined from our measurements. The result is a film morphology which can be seen in figure 7(c): two structurally similar praseodymia species with slightly different film morphologies coexist on top of the silicate.

It can finally be seen that the oxide film thickness decreases during the annealing process. After the first annealing step the PrO_2 and the $PrO_{2-\Delta}$ species lost about 2.4 nm and 1.4 nm of their thickness, respectively. The silicate at the interface increases simultaneously from 2.3 to 4.5 nm. It is obvious that there is a thermally induced atomic diffusion of silicon towards the praseodymia film as reported in [20, 21]. Furthermore, amorphization of the involved film regions occurs, which causes the decreasing crystalline film thickness.

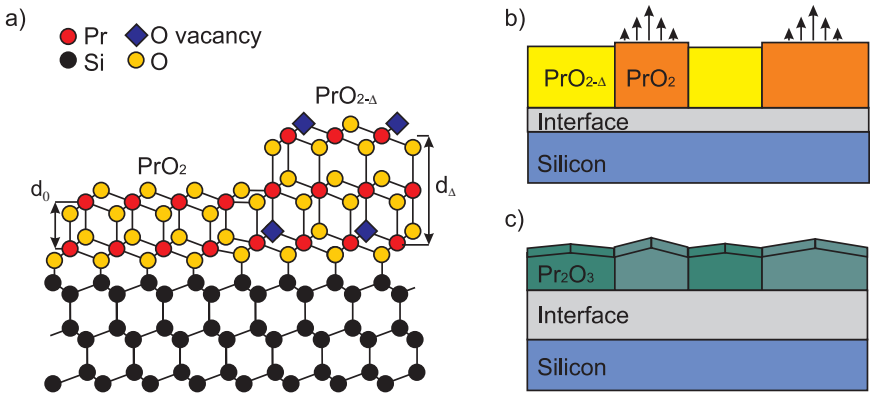

Figure 7. (a) Model of oxide vacancy formation in PrO_2 films. (b) The praseodymia layer system after preparation and (c) after annealing at 300 °C.

Other XRR and XRD experiments with similar PrO_2 samples (not shown here) show, however, that significant silicate growth cannot be detected at annealing temperatures of 200 °C and below. Therefore, the atomic diffusion of silicon into the oxide is suppressed in the low temperature regime. This is because the former silicate interface which is formed during sample preparation serves as a diffusion barrier, so that high annealing temperatures are necessary to transfer silicon into the oxide layer. These experiments also demonstrate a complete phase transition of PrO_2 to cub-Pr_2O_3 after annealing at 200 °C. Based on this fact it can be concluded that the phase transition and silicate growth are independently advancing processes.

Annealing at 600 °C just leads to slightly higher silicate formation at the expense of the oxide layer compared to annealing at 300 °C. It is assumed that the higher annealing temperature does not significantly influence the diffusion length of Si in the silicate film. Finally, it can be expected that the cub-Pr_2O_3 film appears stable with further temperature treatment higher than 300 °C.

Finally, two relaxation processes are visible after annealing at 600 °C. The lattice spacings shift slightly to the value of bulk cub-Pr_2O_3 which points to lateral strain relaxation. However, only one surface species remains as the vanishing of the sharp Lorentzian suggests. This demonstrates that the relaxation at the top of the oxide film is strengthened.

5. Conclusion

The annealing of thin praseodymia films on Si(111) in UHV was investigated with XRD, XRR and SPALEED. The aim was to characterize the annealing process with regard to structural and morphological changes of the crystalline praseodymia film. Our studies show that the phase transition from PrO_2 to cub-Pr_2O_3 for the bulk of the praseodymia film is finished after annealing at 300 °C with a silicon driven increase of the interface silicate at the expense of the crystalline film. Furthermore, two regions with different mosaic spreads form at the film surface due to strain effects of the two laterally pinned species of different stoichiometry. Finally, the film is stable against further temperature treatment up to 600 °C with the exception of relaxation processes at the surface. A two-column model with two laterally existing oxide species was developed to describe the film system during the hole annealing process.

Acknowledgments

The authors would like to acknowledge the Deutsche Forschungsgemeinschaft (DFG) via Graduate College 695 for financial support as well as T Schroeder and A Guissani at the IHP GmbH, Frankfurt (Oder), Germany for kindly providing the investigated samples. XRR and XRD experiments were carried out at the synchrotron light source facilities DORIS III at HASYLAB/DESY. DESY is a member of the Helmholtz Association (HGF). We would like to thank Wolfgang Calibe for assistance in using beamline W1.

References

[1] Thomas J M and Thomas W M 1996 *Principles and Practice of Heterogeneous Catalysis* (Berlin: Wiley–VCH)
[2] Borchert H, Frolova Y V, Kaichev V V, Prosvirin I P, Alikina G M, Lukashevich A I, Zaikovskii V I, Moroz E M, Trukhan S N, Ivanov V P, Paukshtis E A, Bukhtiyarov V I and Sadykov V A 2005 *J. Phys. Chem.* B **108** 5728
[3] Adachi G and Imanaka N 1998 *Chem. Rev.* **98** 1479
[4] Huang S J, Walters A B and Vannice M A 1998 *Appl. Catal.* B **17** 183
[5] Tong Y, Rosynek M P and Lunsford J H 1989 *J. Phys. Chem.* **93** 2896
[6] Asami K, Kusakabe K and Ashi N 1997 *Appl. Catal.* **156** 43
[7] Campbell C T 1997 *Surf. Sci. Rep.* **27** 27
[8] Henry C R 1998 *Surf. Sci. Rep.* **31** 231
[9] Fork D K, Fenner D B and Geballe T H 1990 *J. Appl. Phys.* **68** 4316
[10] Weisemoeller T, Deiter C, Bertram F, Gevers S, Giussani A, Zaumseil P, Schroeder T and Wollschläger J 2008 *Appl. Phys. Lett.* **93** 032905
[11] Tanoto H, Yoon S F, Loke W K, Fitzgerald E A, Dohrman C, Narayanan B, Doan M T and Tung C H 2006 *J. Vac. Sci. Technol.* B **24** 152
[12] Giussani A, Seifarth O, Rodenbach P, Muessig H-J, Zaumseil P, Weisemoeller T, Deiter C, Wollschläger J, Storck P and Schroeder T 2008 *J. Appl. Phys.* **103** 084110
[13] Schroeder T, Lee T-L, Libralesso L, Joumard I and Zegenhagen J 2005 *J. Appl. Phys.* **97** 074906

[14] Hellwege K-H and Hellwege A M (ed) 1975 *Crystal Structure Data of Inorganic Compounds* (*Landolt-Börnstein: Numerical Data and Functional Relationships in Science and Technology (New Series): Group III: Crystal and Solid State Physics* vol 7, (ed) W Pies and A Weiss) (Berlin: Springer)
[15] Lu T-M and Lagally M G 1982 *Surf. Sci.* **120** 47
[16] Schroeder T, Zaumseil P, Weidner G, Wenger C H, Dabrowski J and Muessig H-J 2006 *J. Appl. Phys.* **99** 014101
[17] Jeutter N M, Sidorenko A, Stierle A and Moritz W 2007 *Appl. Phys. Lett.* **90** 062906
[18] Rudenko V S and Boganov A G 1971 *Inorg. Mater. (USSR)* **1** 98 (Engl. Transl.)
[19] Schaefer A, Zielesch V, Schmidt B, Sandell A, Schowalter M, Seifarth O, Walle L E, Schulz Ch, Wollschläger J, Schroeder T, Rosenauer A, Falta J and Bäumer M 2009 at press
[20] Ono H and Katsumata T 2001 *Appl. Phys. Lett.* **78** 1832
[21] Sakai A, Sakashita S, Sakashita M, Yasuda Y, Shigeaki Z and Miyazaki S 2004 *Appl. Phys. Lett.* **85** 5232